Available online at www.sciencedirect.com
ScienceDirect
European Journal of Mechanics B/Fluids 25 (2006) 662–676

Freak waves under the action of wind: experiments and simulations

J. Touboul [a,*], J.P. Giovanangeli [a], C. Kharif [a], E. Pelinovsky [b]

[a] *Institut de Recherche sur les Phénomènes Hors Equilibre (IRPHE), Technopôle de Chateau-Gombert, 49, rue Joliot Curie, BP 146, 13384 Marseille cedex 13, France*

[b] *Laboratory of Hydrophysics and Nonlinear Acoustics, Institute of Applied Physics, 46 Uljanov street, Nizhny Novgorod 603950, Russia*

Received 14 November 2005; accepted 20 February 2006

Available online 5 June 2006

Abstract

The freak wave formation due to the dispersive focusing mechanism is investigated experimentally without wind and in presence of wind. An asymmetric behaviour between the focusing and defocusing stages is found when the wind is blowing over the mechanically generated gravity wave group. This feature corresponds physically to the sustain of the freak wave mechanism on longer periods of time. Furthermore, a weak amplification of the freak wave and a shift in the downstream direction of the point where the waves merge are observed. The experimental results suggest that the Jeffreys' sheltering mechanism could play a key role in the coherence of the group of the freak wave. Hence, the Jeffreys' sheltering theory is introduced in a fully nonlinear model. The results of the numerical simulations confirm that the duration of the freak wave event increases with the wind velocity.

Keywords: Freak waves; Wind interaction; Jeffreys' sheltering mechanism

1. Introduction

Freak, or rogue waves, refer to giant waves appearing suddenly on the sea surface (waves from nowhere). Since they are unpredictable, they are responsible for an important number of marine disasters. Freak waves have been part of the marine folklore for centuries. But confronted to the increasing number of data gathered by oil and shipping industry, the oceanographers began to believe them. A large number of disasters connected to freak waves events have been reported by Mallory, Lawton and others [1,2]. These events took place in a large number of basins, in deep or shallow waters, with or without current.

Several mechanisms have been suggested to explain the formation of rogue waves in so various environments. Among them one can mention the wave-current interaction [3], the geometrical focusing, the dispersive focusing [4,5], the modulational instability or nonlinear focusing [6,7], the soliton collisions [8], etc. More details can be found in a paper by Kharif and Pelinovsky [9].

A statistical approach of the phenomenon has shown that these events could occur really more often than predicted by the linear theory, as it has been pointed out by an increasing number of oceanographers (see [10]). For long-crested waves (narrow angular distribution), a strong correlation is observed between the density increase of large waves and

* Corresponding author.
E-mail address: touboul@irphe.univ-mrs.fr (J. Touboul).

0997-7546/$ – see front matter
doi:10.1016/j.euromechflu.2006.02.006

the spectral change (strong increase of the kurtosis). For short-crested waves (broad angular distribution), the extended Tayfun's distribution approximates quite well the distribution of extreme waves (see Fig. 9 in [10]).

The direct influence of wind has never been taken into account to investigate its role on the dynamics of freak waves. In order to fill in this gap, the paper reports on a series of experiments and numerical simulations designed to analyze the influence of wind on freak waves. Experiments conducted in the Large Air-Sea Interaction Facility (LASIF) of IRPHE, are first described. The results are presented and discussed. The analysis of the mechanism involved in the interaction between wind and freak waves suggests that Jeffreys' sheltering phenomenon could explain some features observed during the experiments. Hence, the Jeffreys' sheltering theory is introduced in a fully nonlinear model. A series of numerical simulations is performed for different values of the wind velocity. Finally, experimental and numerical results are qualitatively compared.

2. Experimental study

2.1. Set-up and experimental conditions

The experiments have been conducted in the large wind-wave tank of IRPHE at Marseille Luminy. Fig. 1 gives a schematic presentation of the facility. It is constituted of a closed loop wind tunnel located over a water tank 40 m long, 1 m deep and 2.6 m wide. The wind tunnel over the water flow is 40 m long, 3.2 m wide and 1.6 m high. The blower allows to produce wind speeds up to 14 m/s and a computer-controlled wave maker submerged under the upstream beach can generate regular or random waves in a frequency range from 0.5 Hz to 2 Hz. Particular attention has been taken to simulate pure logarithmic mean wind profile with constant shear layer over the water surface. A trolley installed in the test section allows to locate probes at different fetches all along the facility. The water surface elevation is determined by using three capacitive wave gauges of 0.3 mm outer diameter with DANTEC model 55E capacitance measuring units. A wave gauge is located at a fixed fetch of 1 m from the upstream beach. The other wave gauges are installed on the trolley in order to determine the water surface elevation at different fetches from the upstream beach. The typical sensitivity of the wave probes is of order 0.6 V/cm.

Freak waves are generated by means of a spatio-temporal focusing mechanism. This mechanism is based upon the dispersive behaviour of water waves. A linear approach of the problem would lead to consider sea surface as a superposition of linear waves of frequencies $\omega(x,t)$. According to Whitham (see [11]), the spatio-temporal evolution of the frequency of these components is governed by the following hyperbolic equation

$$\frac{\partial\omega}{\partial t} + c_{\mathrm{gr}}(\omega)\frac{\partial\omega}{\partial x} = 0 \tag{1}$$

where c_{gr} is the group velocity. This equation can be solved by using the method of characteristics. Its solution is

$$\omega(x,t) = \omega_0(\tau), \quad v_g(\tau) = c_{\mathrm{gr}}\big(\omega_0(\tau)\big) \quad \text{on } t = \tau + x/v_g(\tau) \tag{2}$$

where ω_0 corresponds to the temporal frequency distribution of the wave train at $x = 0$. By differentiating the frequency, one obtains

$$\frac{\partial\omega}{\partial t} = \frac{v_g^2\,\mathrm{d}\omega_0/\mathrm{d}\tau}{v_g^2 - x\,\mathrm{d}v_g/\mathrm{d}\tau} \tag{3}$$

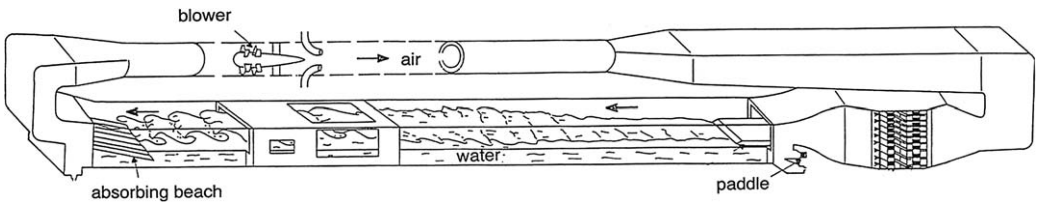

Fig. 1. A schematic representation of the large air-sea interactions facility.

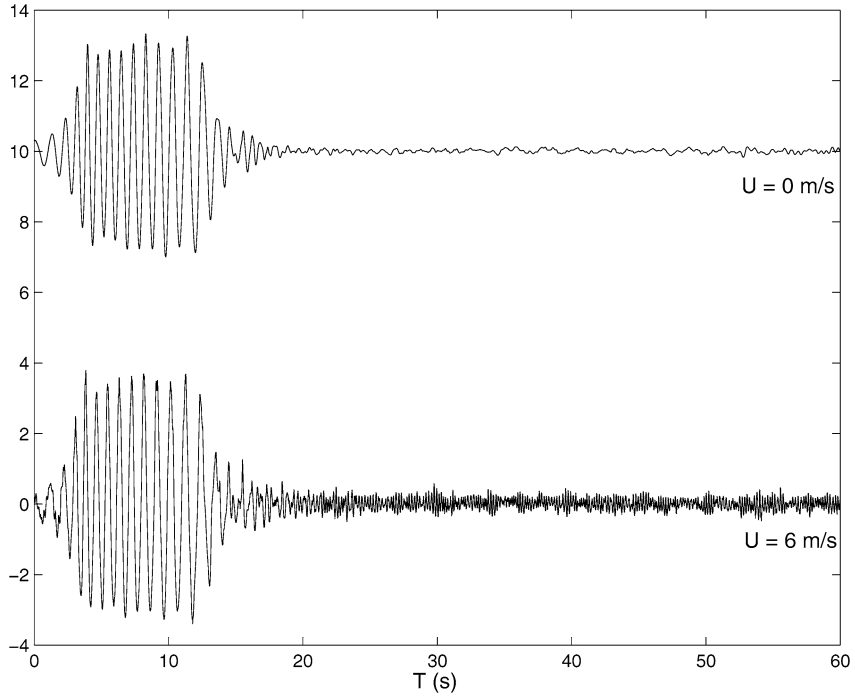

Fig. 2. Surface elevation (in cm) at fetch $X = 1$ m, for wind speeds $U = 0$ and 6 m/s.

and one can notice that the case $\mathrm{d}v_g/\mathrm{d}\tau > 0$, which corresponds to the case of short waves emitted before longer waves, leads to a singularity. This singularity corresponds to the focusing of several waves at $t = T_{f_{\mathrm{th}}}$ and $x = X_{f_{\mathrm{th}}}$. For infinite depth, the frequency to impose to a wave maker located at $x = 0$ is given by

$$\omega(0,t) = \frac{g}{2}\frac{T_{f_{\mathrm{th}}} - t}{X_{f_{\mathrm{th}}}} \tag{4}$$

where $X_{f_{\mathrm{th}}}$ and $T_{f_{\mathrm{th}}}$ are the coordinates of the focusing point in the $(x$–$t)$ plane

$$\begin{aligned} T_{f_{\mathrm{th}}} &= T\frac{f_{\max}}{f_{\max} - f_{\min}}, \\ X_{f_{\mathrm{th}}} &= \frac{gT}{4\pi}\frac{1}{f_{\max} - f_{\min}} \end{aligned} \tag{5}$$

and g is the acceleration due to gravity.

Experimentally, the values $f_{\max} = 1.3$ Hz and $f_{\min} = 0.8$ Hz correspond to the maximal and minimal frequencies of the wave maker and $T = 10$ s is the duration of the wave generation. The surface elevation given by the probe located at 1 m from the upstream beach is presented in Fig. 2. From these data we find that $T_{f_{\mathrm{th}}} = 26$ s and $X_{f_{\mathrm{th}}} = 17$ m while the experimental values are $T_{f_{\mathrm{exp}}} = 26$ s and $X_{f_{\mathrm{exp}}} = 20$ m (see Fig. 3). Experimental data show a good agreement with the linear theory. The slight difference observed between the theoretical and experimental values of X_f is mainly due to the nonlinearity of the experimental wave train.

The focusing experiments are performed with and without wind. The same initial wave train is propagated freely (without wind), and under the action of wind for several values of the wind velocity equal to $U = 4$ m/s, 5 m/s, 6 m/s, 8 m/s and 10 m/s. When the wind blows, the focusing wave train is generated once wind waves have developed. For each value of the mean wind velocity U the water surface elevation is measured at 1 m fetch and at different fetches between 3 m and 35 m. The wave maker is driven by an analog electronic signal, in order to produce this signal linearly varying with time from 1.3 Hz to 0.8 Hz in 10 s, with an almost constant amplitude of the displacement. The fetch is measured from the entrance of the wave-tank where the air flow meets the water surface i.e. at the end of the upstream beach. The wave maker is totally submerged, in order to avoid perturbation of the air flow which could be induced by its displacement.

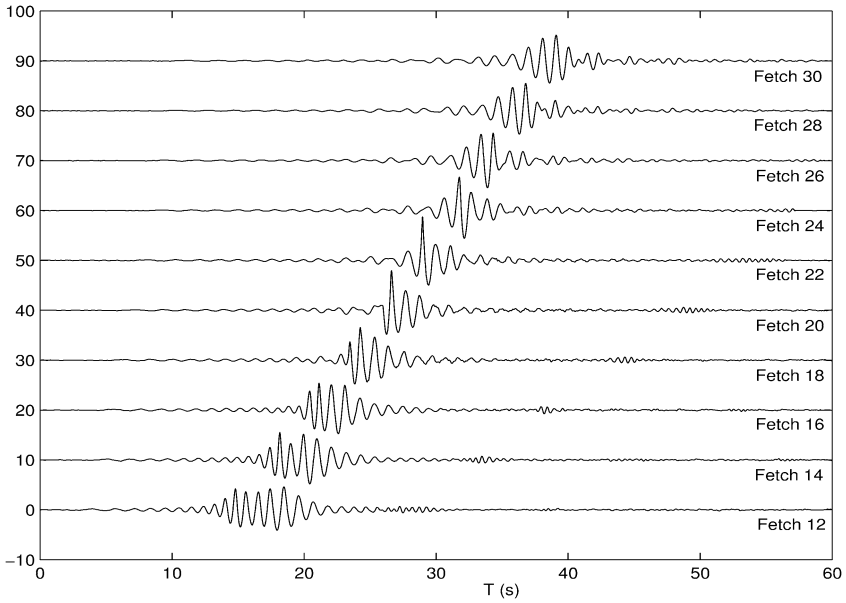

Fig. 3. Surface elevation (in cm) at several fetches (in m), for wind speed $U = 0$ m/s, as a function of time.

Table 1
The r.m.s. elevation for different values of the wind velocity at fetch 1 m

Wind velocity (m/s)	$\sqrt{\langle \eta^2 \rangle}$ (cm)
0	1.88
4	1.88
5	1.87
6	1.88
8	1.87
10	1.88

To ensure the repeatability of the experimental conditions under the wind action, the water elevations at 1 m were recorded with and without wind. Fig. 2 shows two time-series of this probe, recorded with no wind, and under a wind speed $U = 6$ m/s. The probe record corresponding to a wind of 6 m/s is artificially increased by 10 cm, for more clarity of the figure. We see that the two signals are very similar, since frequency properties, phases and duration are maintained. Some weak differences in amplitude are locally observed. Table 1 shows the root mean square of the elevation $\eta(x, t)$ obtained at fetch 1 m for different wind speeds. It is clear from these data that no significant variations are observed, and the experiment is considered to be repeatable in presence of wind. Results of these experiments are presented in the following subsection.

2.2. Experimental results

Fig. 3 presents the time series of the water surface elevation $\eta(x, t)$ at different fetches for $U = 0$ m/s. For sake of clarity, as it has been done for Fig. 2, the probes records given here are recursively increased by 10 cm. As predicted by the linear theory of the free deep-water waves (no wind), dispersion leads short waves to propagate slower than long waves, and as a matter of fact, the waves focus at a precise distance leading to the occurrence of a large amplitude freak wave. Downstream the point of focusing, the amplitude of the group decreases rapidly (defocusing).

Fig. 4 shows the same time series of $\eta(x, t)$, at several values of the fetch x, and for a wind speed $U = 6$ m/s. The wave groups mechanically generated by the wave maker are identical to those used in the case without wind (see Fig. 2). Whatever, some differences appear in the time–space evolution of the focusing wave train.

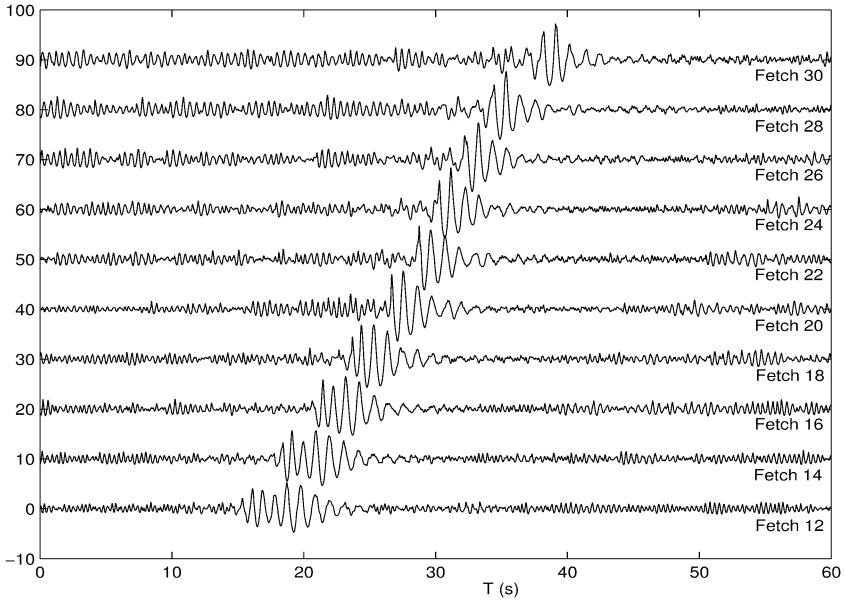

Fig. 4. Surface elevation (in cm) at several fetches (in m), for wind speed $U = 6$ m/s, as a function of time.

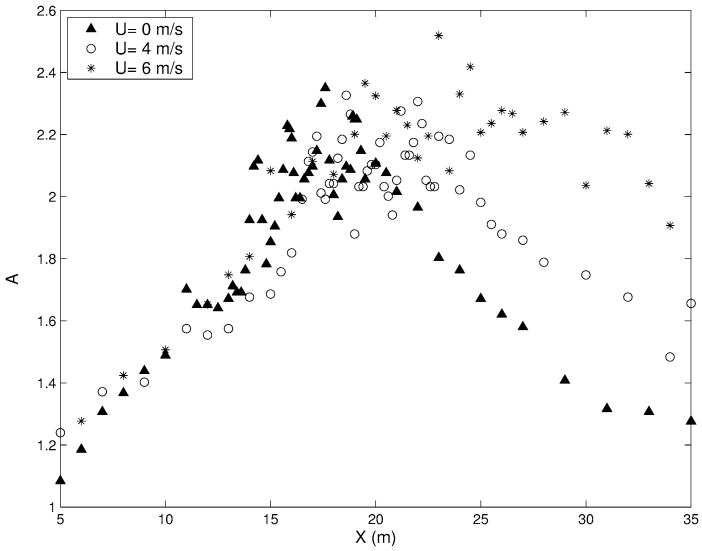

Fig. 5. Evolution of the amplification factor $A(x, U)$ as a function of the distance (in m), for several values of the wind speed.

For each value of the wind velocity, the amplification factor $A(x, U)$ of the group between fetches x and 1 m can be defined as

$$A(x, U) = \frac{H_{\max}(x, U)}{H_{\text{ref}}} \tag{6}$$

where $H_{\max}(x, U)$ is the maximal height between two consecutive crest and through in the transient group. The height, H_{ref}, of the quasi uniform wave train generated at the entrance of the tank is measured at 1 m. The mean height crest to through is $H_{\text{ref}} = 6.13$ cm.

Fig. 5 gives this amplification factor as a function of the distance from the upstream beach for various values of the wind velocity, equal to 0 m/s, 4 m/s and 6 m/s. This figure shows that the effect of the wind is twofold: (i) it increases weakly the amplification factor, and (ii) it shifts downstream the focusing point (caustic). Moreover,

contrary to the case without wind, an asymmetry appears between focusing and defocusing stages. The slope of the curves corresponding to defocusing changes. One can observe that the freak wave criterium ($A > 2$) is satisfied for a longer period of time. The effect of the wind on the freak wave is to shift the focusing point downstream, and to increase slightly its amplitude. It is also interesting to emphasize that the freak wave criterium is satisfied for a longer distance, while the wind velocity increases.

To better understand the time–space evolution of the wave group with and without wind, the time series are analyzed by means of a wavelet analysis. Fig. 6 displays the wavelet analysis at several fetches, without wind. It shows the time-frequency evolution of the wave group as it propagates downstream the wave tank. At small fetches, the waves of high frequencies are in front of the group and the waves of lower frequencies at its back. As it propagates downstream, a focusing and defocusing process is observed. Downstream the focusing point, the waves of low frequencies are in front of the group, and the high frequencies at its back. In Fig. 7 is shown the wavelet analysis of probe records at the same fetches, for a wind speed of 6 m/s. Contrary to the case without wind, the focusing point seems to be shifted downstream the wave tank, confirming what we observe in Fig. 5. The freak wave mechanism is sustained longer. We note that the coherence of the group is maintained longer. This could explain the asymmetry observed in the amplification curves.

We observe in Figs. 4 and 7, that the background wind waves are suppressed by the freak wave. The phenomenon of high frequency waves suppressed by strongly nonlinear low frequency waves has been investigated by Balk [12]. He showed that the effect of the long wave is to transport the short wave action to high wave numbers, where high dissipation occurs.

To summarize the main experimental results we can claim that the effect of wind on the freak wave mechanism is to shift the focusing point downstream, to increase its amplitude and lifetime due to an asymmetry of the amplification curve. Figs. 6 and 7 demonstrate that the effect of the wind is to transform the short group containing the freak wave into a long-lived short group. The effect of the wind is to delay the defocusing stage.

3. Wind action modeling

As it has been mentioned in the description of the experimental setup, the focusing wave group is generated only once the wind is established in the wind tunnel. This means that the waves generated mechanically propagate on a current induced by the wind near the water surface. In a recent approach, Giovanangeli et al. [13] suggested that the presence of this current could explain the shift of the focusing point downstream. The comparison with a linear theory based on the parabolic equation for the evolution of the amplitude, showed that indeed the shift was due to the action of the current. A good agreement between experimental and theoretical amplification was obtained. Unfortunately, the linear theory was unable to explain the asymmetry of the amplification curve observed during the experiments.

Since the asymmetry observed experimentally in the amplification curve cannot be explained by the effect of the current induced by the wind one should find an explanation in the direct action of the wind on the freak wave. To model this interaction, two mechanisms can be considered: the Miles' mechanism, and the Jeffreys' sheltering mechanism. The Miles' mechanism is a quasi laminar model of the transfer of energy to a surface wave from a turbulent shear flow [14]. The Jeffreys' sheltering mechanism assumes that this transfer is due to the air flow separation occurring over very steep waves [15,16].

To see what is the dominant phenomenon prevailing in our experiments, one can calculate the characteristic time scale of each mechanism. According to the Jeffrey's theory the energy flux for a monochromatic wave is given by

$$\frac{\partial E}{\partial t} = \frac{1}{2} S \rho_a (U - c_\varphi)^2 a^2 k^2 c_\varphi \tag{7}$$

where S is the Jeffreys' sheltering coefficient, ρ_a is the atmospheric density, U is the mean wind velocity, c_φ is the wave phase velocity, a and k are the amplitude and wavenumber of the wave respectively, $E = \rho_w g a^2/2$ is the mean wave energy (ρ_w is the water density).

The normalized growth rate is given by

$$\frac{1}{E}\frac{\partial E}{\partial t} = S \frac{\rho_a}{\rho_w} \frac{(U - c_\varphi)^2}{c_\varphi^2} \omega = \Gamma_{\text{Jeffreys}} \tag{8}$$

where the wave frequency is $\omega = \sqrt{gk}$.

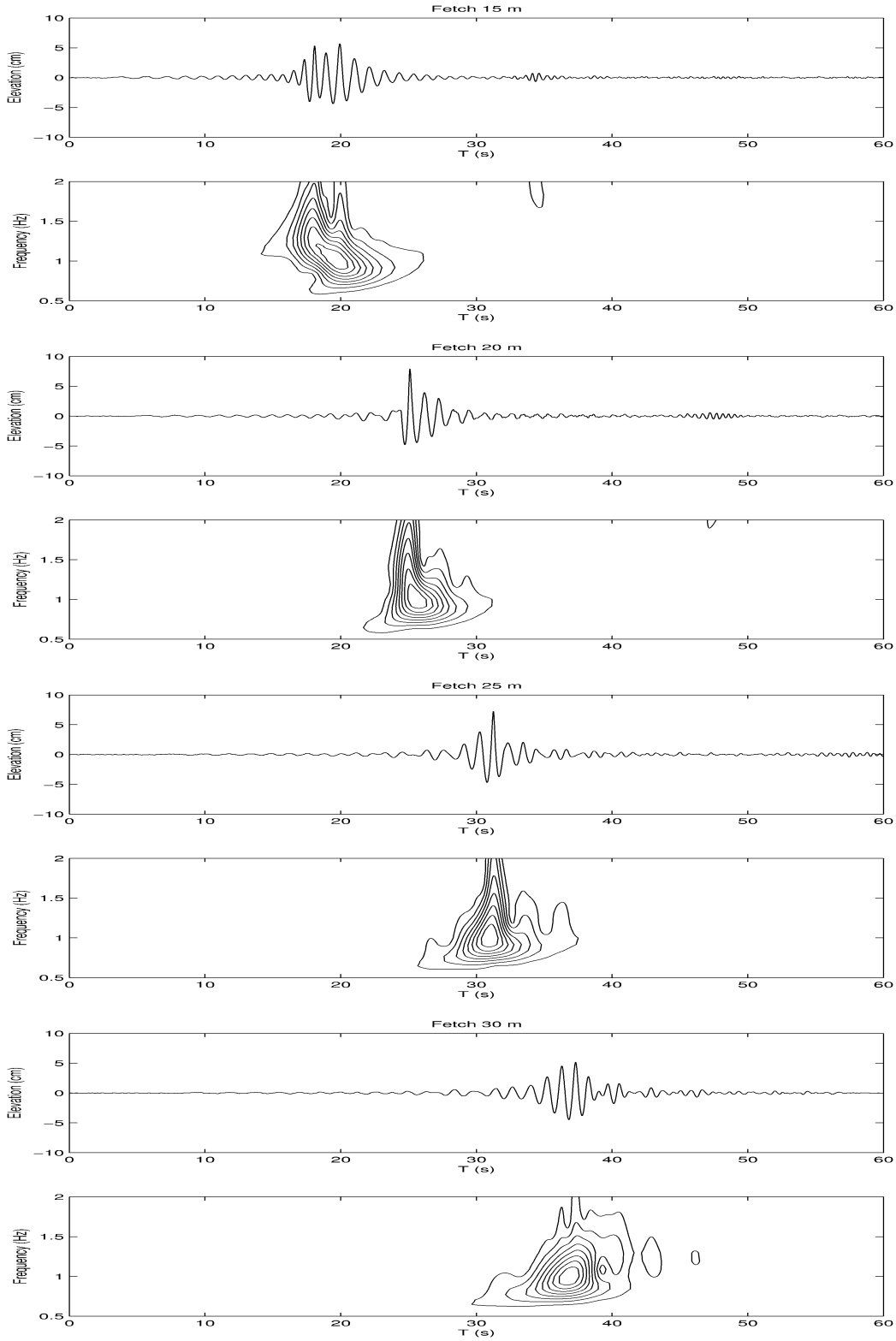

Fig. 6. Wavelet analysis of probe records for fetches $x = 15$, 20, 25 and 30 m for a wind speed value of $U = 0$ m/s.

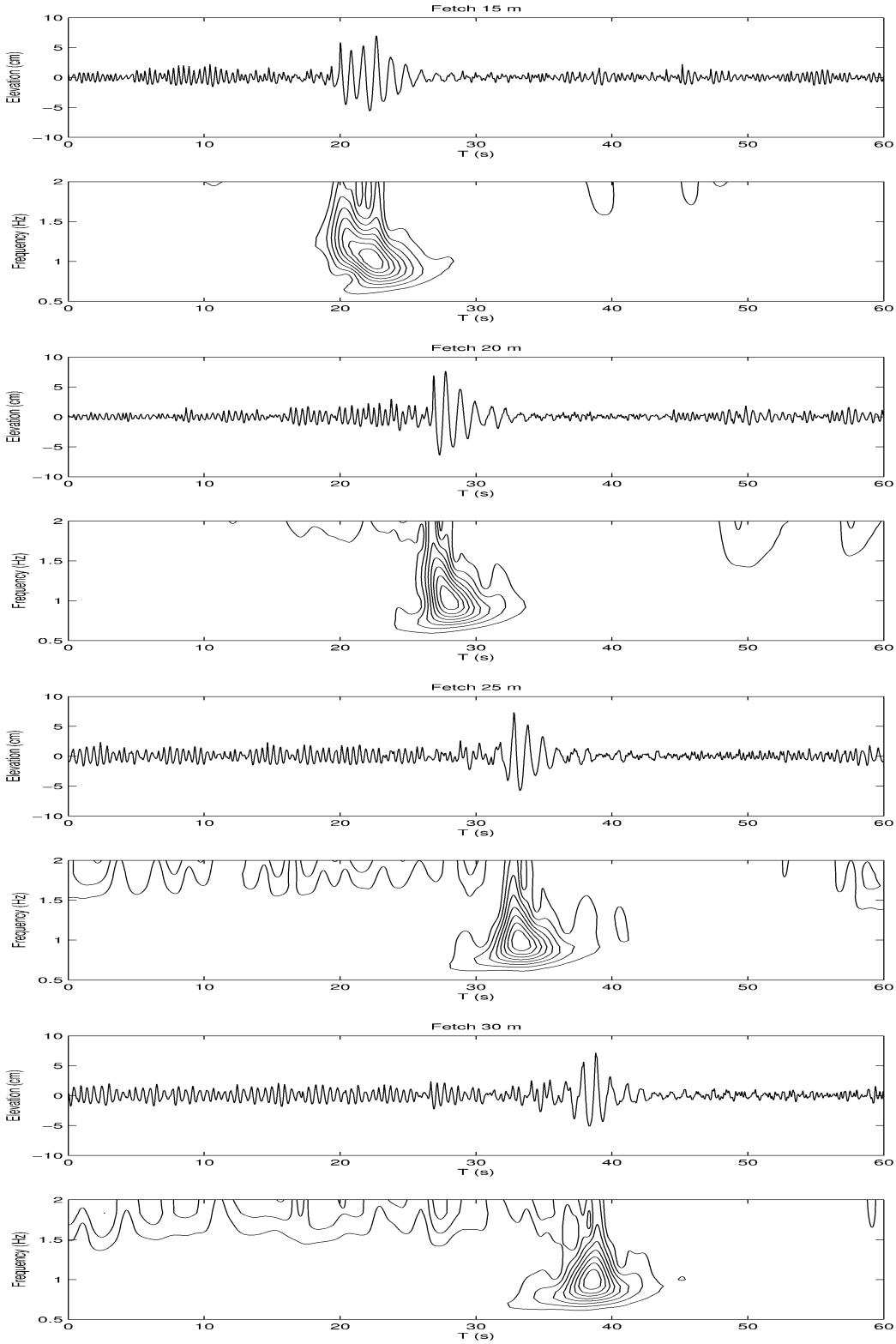

Fig. 7. Wavelet analysis of probe records for fetches $x = 15$, 20, 25, and 30 m, for a wind speed value of $U = 6$ m/s.

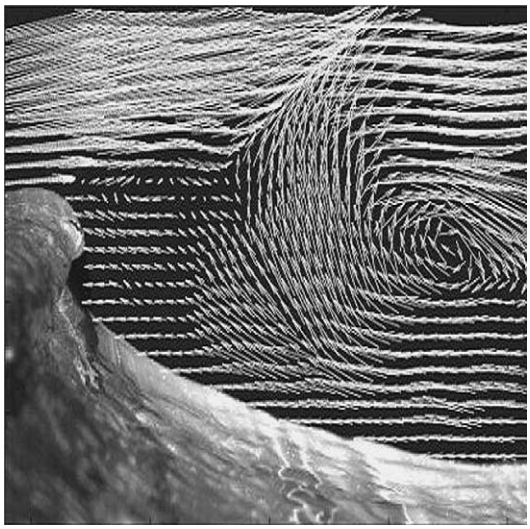

Fig. 8. Air flow separation observed by PIV over a breaking wave (Reul et al., [17]).

Based upon the same idea, the normalized growth rate relative to the Miles' mechanism is written as follows

$$\frac{1}{E}\frac{\partial E}{\partial t} = \frac{\rho_a}{\rho_w}\frac{\beta}{\kappa^2}\frac{U_*^2}{c_\varphi^2}\omega = \Gamma_{\text{Miles}} \tag{9}$$

where κ is von Karman's constant, β is the energy-transfer parameter of Miles and U_* is the friction velocity.

The ratio of the two characteristic time scales is given by

$$\frac{\Gamma_{\text{Jeffreys}}}{\Gamma_{\text{Miles}}} = S\frac{\kappa^2}{\beta}\frac{(U-c_\varphi)^2}{U_*^2}. \tag{10}$$

The sheltering coefficient, $S = 0.5$, was calculated from experimental data. The friction velocity is $U_* = U\sqrt{C_d}$ where the measured drag coefficient is $C_d = 0.004$. The energy transfer parameter β is a function of the wave age obtained from Fig. 1 of [14]. For U varying from 4 m/s to 8 m/s, and by assuming that the freak wave generated experimentally presents a peak at 1 Hz, it is found that the Miles' characteristic time scale is roughly three times the Jeffreys' characteristic time scale. Furthermore, Fig. 5 shows that the amplification factor does not depend on the wind velocity during the focusing stage up to the freak wave occurrence. The asymmetry which develops rapidly is due to a fast phenomenon such as flow separation occurring on the leeward side of wave crests. The picture presented in Fig. 8 was provided by Reul et al. [17] who performed PIV measurements of the air flow over a breaking wave. They showed that above the leeward face of a nearly breaking wave, i.e. a high steepness wave, a well organized vortex appears due to an air flow separation process. Moreover Banner [18] demonstrated that air flow separation is responsible for large increments in the form drag. These remarks lead us to consider that Jeffreys' mechanism is more relevant than the Miles' mechanism to describe the air sea interaction process observed in the present experiments.

Under the assumption of the air flow separation, Jeffreys suggested that the air flow pressure at the interface, $z = \eta(x,t)$, is related to the local wave slope, according to the following expression

$$p = \rho_a S(U-c_\varphi)^2\frac{\partial \eta}{\partial x}. \tag{11}$$

He considered that the out of phase pressure-surface elevation variations could lead to wave growth. We use this approach and apply the Jeffreys' mechanism when the wave steepness is larger than a given threshold. Hence, we introduce a critical value of the local slope η_{x_c}, above which an energy transfer from the wind to the waves occurs. The corresponding pressure distribution at the surface given by Eq. (11) is shown in Fig. 9. For each wave, the maximal local slope is computed, and the pressure distribution on the surface of the wave is given by

$$\begin{cases} p(x) = 0 & \text{if } \eta_{x_{\max}} < \eta_{x_c}, \\ p(x) = \rho_a S(U-c_\varphi)^2\frac{\partial \eta}{\partial x}(x) & \text{if } \eta_{x_{\max}} \geqslant \eta_{x_c}. \end{cases} \tag{12}$$

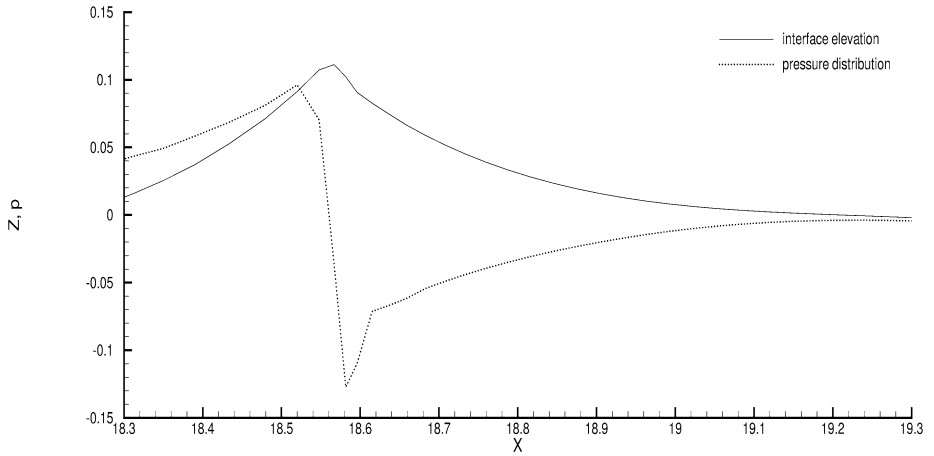

Fig. 9. Pressure distribution (dotted line, given in 10^{-1} Hpa) on the interface (solid line, given in m) in the model.

This critical value η_{x_c} is arbitrarily chosen as a parameter, varying from 0.44 to 0.57. These values correspond to angles close to 30 degrees. One can note that this value corresponds to the maximal local slope reached by a Stokes wave. The Stokes' corner presenting exactly this value. In this way the Jeffreys' sheltering mechanism works when the critical steepness of the surface is locally reached. The transfer of energy from the wind to the water waves stops as soon as the maximal local steepness becomes lower than η_{x_c}.

4. Numerical study

4.1. Mathematical formulation and numerical modeling

4.1.1. Mathematical formulation

The problem is solved by assuming the fluid to be inviscid, incompressible, and the motion irrotational. Hence, the velocity field is given by $\vec{u} = \nabla\phi$ where the velocity potential $\phi(x, z, t)$ satisfies the Laplace's equation

$$\Delta\phi = 0. \tag{13}$$

Eq. (13) is solved within a domain bounded by the fluid interface and solid boundaries of the numerical wave tank. The boundary conditions are defined below.

The impermeability condition writes

$$\nabla\phi \cdot \vec{n} = \vec{V} \cdot \vec{n} \quad \text{on } \partial\Omega_B \tag{14}$$

where $\partial\Omega_B$ is the solid boundaries, $\vec{V}$ is the velocity of these solid boundaries, set equal to zero on the walls of the wave tank, and equal to the velocity of the paddle at any point of the wave maker and $\vec{n}$ is the unit normal vector to the boundaries.

A Lagrangian description of the free surface is used

$$\begin{aligned} \frac{Dx}{Dt} &= \frac{\partial\phi}{\partial x}, \\ \frac{Dz}{Dt} &= \frac{\partial\phi}{\partial z} \end{aligned} \tag{15}$$

where $\frac{D}{Dt} = \frac{\partial}{\partial t} + \nabla\phi \cdot \nabla$.

The dynamic free surface condition states that the pressure at the surface is equal to the atmospheric pressure:

$$\frac{D\phi}{Dt} = \frac{1}{2}\nabla\phi^2 - gz - p, \tag{16}$$

where $p(x,t)$ is given by Eq. (11). Thus the problem to be solved is

$$\begin{cases} \Delta\phi = 0 & \text{in the fluid domain,} \\ \dfrac{\partial\phi}{\partial n} = \vec{V}\cdot\vec{n} & \text{on the solid boundaries,} \\ \dfrac{D\phi}{Dt} = \dfrac{\nabla\phi^2}{2} - gz - p, & \\ \dfrac{Dx}{Dt} = \dfrac{\partial\phi}{\partial x} & \text{on the free surface,} \\ \dfrac{Dz}{Dt} = \dfrac{\partial\phi}{\partial z}. & \end{cases} \tag{17}$$

4.1.2. Numerical modeling

The equations are solved using a boundary integral equation method (BIEM) and a mixed Euler Lagrange (MEL) time marching scheme. The Green's second identity is used to solve Laplace's equation

$$\int_{\partial\Omega} \phi(P)\frac{\partial G}{\partial n}(P,Q)\,\mathrm{d}l - \int_{\partial\Omega} \frac{\partial\phi}{\partial n}(P)G(P,Q)\,\mathrm{d}l = c(Q)\phi(Q) \tag{18}$$

for the velocity potential. Here $\partial\Omega = \partial\Omega_F \cup \partial\Omega_B$, where $\partial\Omega_F$ is the free surface boundary, and $\partial\Omega_B$ is the body boundary. Thus, $\partial\Omega$ is the fluid domain boundary. G is the free space Green's function. The unit normal vector $\vec{n}$ points outside the fluid domain. The angle $c(Q)$ is defined as

$$c(Q) = \begin{cases} 0 & \text{if } Q \text{ is outside the fluid domain,} \\ \alpha & \text{if } Q \text{ is on the boundary,} \\ -2\pi & \text{if } Q \text{ is inside the fluid domain} \end{cases} \tag{19}$$

where α is the inner angle relative to the fluid domain at point Q along the boundary. Eq. (18) can be rewritten as follows

$$\alpha\phi - \int_{\partial\Omega_F} \phi(P)\frac{\partial G}{\partial n}(P,Q)\,\mathrm{d}l + \int_{\partial\Omega_B} \frac{\partial\phi}{\partial n}(P)G(P,Q)\,\mathrm{d}l = \int_{\partial\Omega_B} \phi(P)\frac{\partial G}{\partial n}(P,Q)\,\mathrm{d}l - \int_{\partial\Omega_F} \frac{\partial\phi}{\partial n}(P)G(P,Q)\,\mathrm{d}l$$

for $Q \in \partial\Omega_F$, and

$$\int_{\partial\Omega_F} \phi(P)\frac{\partial G}{\partial n}(P,Q)\,\mathrm{d}l + \int_{\partial\Omega_B} \frac{\partial\phi}{\partial n}(P)G(P,Q)\,\mathrm{d}l = \alpha\phi + \int_{\partial\Omega_B} \phi(P)\frac{\partial G}{\partial n}(P,Q)\,\mathrm{d}l - \int_{\partial\Omega_F} \frac{\partial\phi}{\partial n}(P)G(P,Q)\,\mathrm{d}l$$

for $Q \in \partial\Omega_B$.

The unknowns are $\frac{\partial\phi}{\partial n}$ on $\partial\Omega_F$ and ϕ on $\partial\Omega_B$ in the integrands of the right-hand side of the above equations. These equations satisfied at a discrete set of N nodes on the boundaries, are transformed into a linear system of algebraic equations for a finite number of unknowns (see [19,20]).

4.2. Tests of convergence

In order to check the convergence of the numerical scheme we have performed a series of numerical simulations for different values of the number of meshes N. A modulated motion is imposed to the wave maker generating a focusing modulated wave train. An absorbing beach located at the end of the wave tank dissipates the incident wave energy. For more details about the principle of the experiment see Section 4.4.1. To avoid numerical instability the grid spacing Δx and time increment Δt have been chosen to satisfy the following Courant relation derived from the linearized surface conditions

$$\Delta t^2 \leqslant \frac{8\Delta x}{\pi g}. \tag{20}$$

Table 2 displays the values of the maximum of elevation at the focusing fetch for increasing values of the number of meshes. For $N = 2000$ the accuracy of the computations is less than 10^{-3}.

Table 2
Maximum elevation of the surface as a function of N, the number of meshes

N	$\eta_{\max}$
500	0.076409205
750	0.092047992
1000	0.098460514
1250	0.101706569
1500	0.103529434
1750	0.104587033
2000	0.105057848

4.3. Verification of the method

Following Dommermuth et al. [21] who conducted numerical simulations and experiments of focusing gravity waves in infinite depth, we reproduced numerically their experimental setup by adopting similar numerical parameters.

4.3.1. Principle of the simulations

The spatio-temporal focusing mechanism is simulated in a 25 m long wave tank, 0.7 m wide, and 0.6 m deep. The piston wave maker is moving periodically with the velocity

$$U(t) = \sum_{n=1}^{72} U_n \cos(\omega_n t - \theta_n), \tag{21}$$

where the coefficients U_n, ω_n and θ_n are the parameters of the initial value signal. These parameters can be found in [21]. This corresponds to the spatio-temporal focusing mechanism. Short waves are emitted first, followed by longer waves. All waves meet at a point of the wave tank. Using these data, we have reproduced the same numerical conditions.

For these simulations, Dommermuth et al. used 250 meshes on the free surface. A dynamic regridding was performed every five time steps. They used a dynamic time step to perform the time integration, almost constant and close to 0.05 s before the occurrence of breaking. When breaking occurred, a mesh refinement was iteratively performed, and then the time step decreased.

To compare with their results, the time step Δt is fixed equal to 0.05 s, and reduced when approaching breaking. we use 250 meshes on the free surface before breaking, and mesh refinement is applied iteratively.

4.3.2. Numerical results

Comparison between our numerical simulations and the results obtained by Dommermuth et al. before breaking stage is presented in Fig. 10.

These curves show the time records of probes located along the tank, at fetches equal to (a): 3.17 m, (b): 5.00 m, (c): 6.67 m, (d): 9.17 m, and (e): 10.83 m. The origin of the tank corresponds to the wave maker position at rest. Fig. 10 displays the focusing of several waves into an extreme wave. One can notice that the agreement is quite good, but some differences appear when the wave group focuses, and begins to break.

4.4. Effect of the wind: numerical simulations

4.4.1. Principle of the experiment

A 2D numerical wave tank simulating the Large Air-Sea Interaction Facility has been considered. The tank has a length of 40 m, and a depth of 1 m. A focusing wave train is generated by a piston wave maker, leading to the formation of a rogue wave followed by a defocusing stage. The free surface, and the solid walls (downstream wall, bottom and wave maker) are discretized by 1300, and 700 meshes respectively, uniformly distributed.

The time integration is performed by using a RK4 scheme, with a constant time step of 0.01 s. The focusing process is studied successively with and without wind.

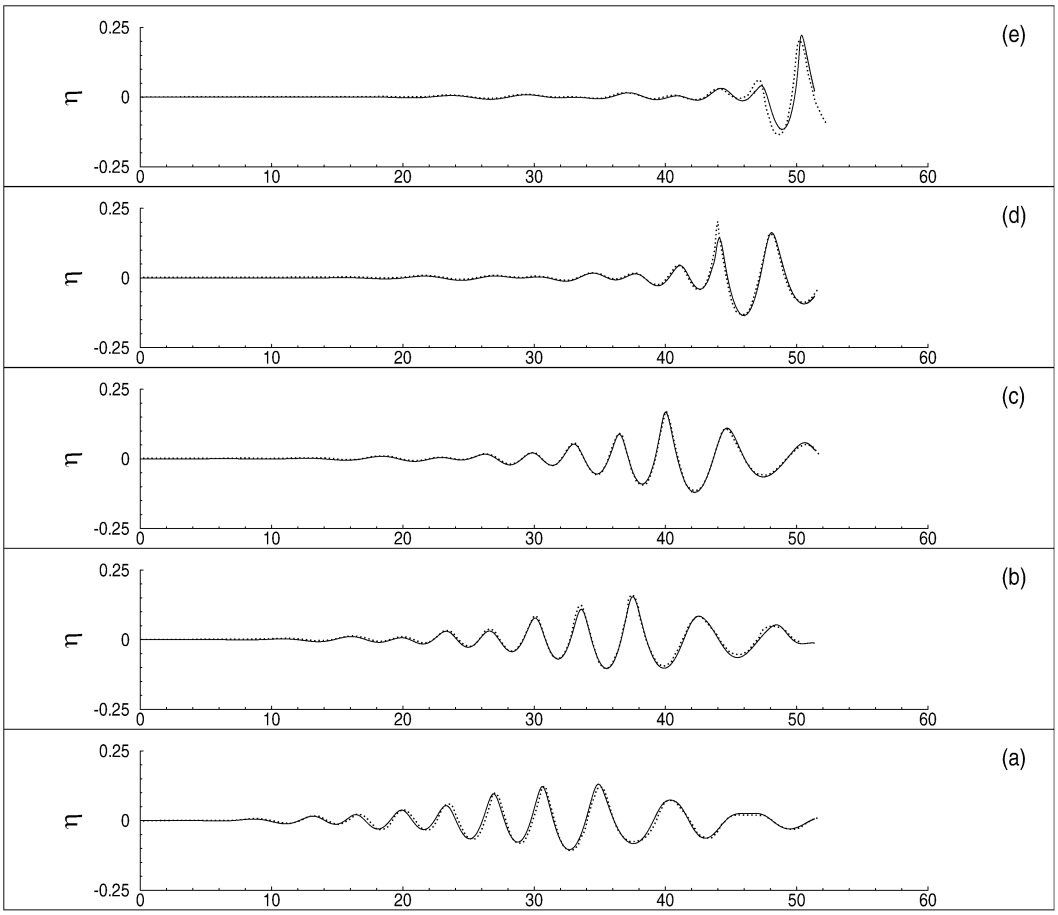

Fig. 10. Numerical results of the spatio-temporal focusing: elevation as a function of time for fetches (a): 3.17 m, (b): 5.00 m, (c): 6.67 m, (d): 9.17 m, and (e): 10.83 m. Dotted line: present results. Solid line: from Dommermuth et al.

4.4.2. Numerical results

The numerical simulations have been run for several values of the critical wave slope η_{x_c}, and wind velocity.

Fig. 11 shows the spatial evolution of the amplification factor computed numerically by using Eq. (6). These curves plotted for three values of the wind velocity, $U = 0$ m/s, 4 m/s and 6 m/s present the same behavior than those in Fig. 5 and emphasize again the asymmetry found in the experiments. Herein, the critical slope beyond which the wind forcing is applied is $\eta_{x_c} = 0.5$. One can notice that the effect of the wind is not sufficient to increase the amplification of the freak wave. A very weak increase of the amplification factor is observed in presence of wind. The increase of the amplification due to the wind is significantly larger in the experiments. This feature will be discussed later. However, one can observe a significant asymmetry between the focusing and defocusing stages of the wave train. This asymmetry results in an increase of the life time of the freak wave event. Furthermore, a comparison between Fig. 11 and Fig. 5 shows that the numerical maxima of the amplification factor are larger than those obtained experimentally. This can be due in part to spilling breaking events which were observed in the experiments, resulting in dissipation of energy, and in saturation in the growth of the amplification factor. The comparison between experimental and numerical results should remain qualitative since the initial conditions used in the experiments and simulations are different. The fact that no downstream shifting of the focusing point is observed in the numerical simulations is due to the absence of current in the model.

It is important to emphasize that the transfer of energy from the wind to the water waves depends mainly on two parameters, which are the wind velocity, and its duration depending on the critical parameter η_{x_c}. Fig. 12 shows the duration of the transfer of energy as a function of the critical parameter η_{x_c} for several values of the wind velocity. The curve $U = 0$ m/s which corresponds to no wind shows the time during which the group presents a local slope

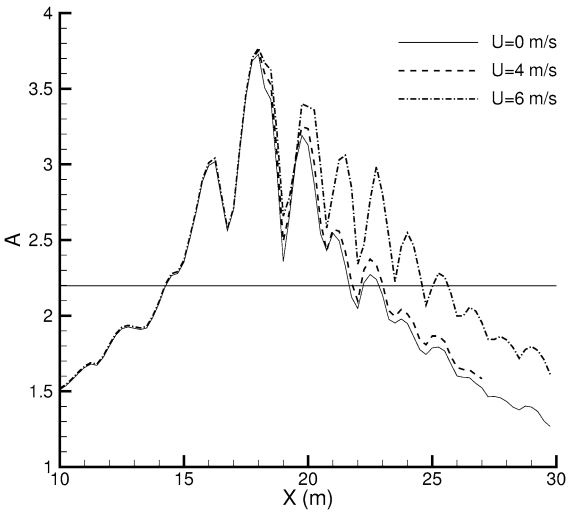

Fig. 11. Evolution of the numerical amplification factor $A(x, U)$ as a function of fetch (in m) and for wind speeds $U = 0$, 4 and 6 m/s. The critical slope is $\eta_{x_c} = 0.5$.

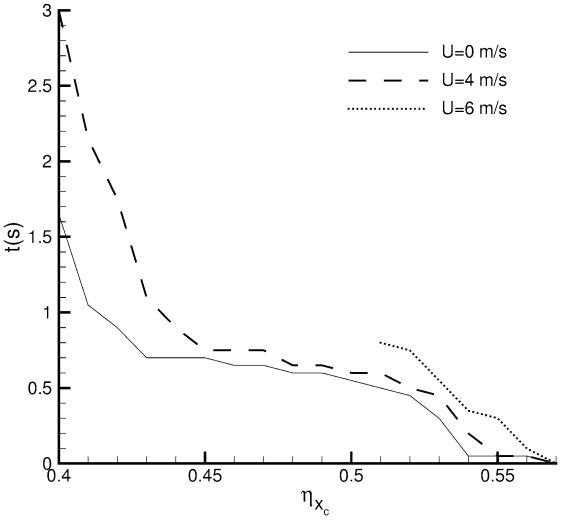

Fig. 12. Duration of energy transfer from wind as a function of the critical slope η_{x_c}.

larger than a critical value. One can notice that the critical wave slope $\eta_{x_c} = 0.57$ corresponds to a value that is never exceeded during the simulation without wind, meaning that no forcing can exist, whatever the wind velocity is. Curves relative to wind velocity values of $U = 4$ m/s and 6 m/s correspond to the time during which a transfer of energy is imposed. The duration of transfer of energy increases wind velocity, nevertheless it is seen from the latter curve that it stops due to the occurrence of breaking.

The wind velocity and threshold critical wave slope have a strong influence on the duration of the transfer of energy from the wind to the waves. For a given critical wave slope, this time increases significantly as the wind velocity increases. Owing to the large difference existing between air and water densities, the time of forcing corresponding to the wind input is not long enough to amplify significantly the height of the freak wave event. The main effect of the sheltering mechanism is to sustain the coherence of the short group involving the freak wave.

5. Conclusions

The direct effect of the wind on a freak wave event generated by means of a dispersive spatio-temporal mechanism has been investigated experimentally and numerically.

The experiments have shown that, in presence of wind, the focusing point is shifted downstream, which is due to the action of the current induced by the wind (see Giovanangeli et al. [13]). A weak increase of the freak wave height, and an asymmetry in the amplification curve occurs in presence of wind. This asymmetry results in an enhancement of the life time of the freak wave event.

The mechanism suggested to explain the energy transfer needed to sustain the envelope of the group involving the freak wave event is the Jeffreys' sheltering mechanism. This phenomenon is due to the air flow separation process occurring over very steep waves (see [15–17]). Following Jeffreys we expressed the normal wind tension at the sea surface as a sum of two terms, one being a constant reference to atmospheric pressure and the other to the wind pressure. The numerical results presented here have demonstrated that this mechanism may explain the sustain of the freak wave event.

Both experimental and numerical results are in qualitative good agreement even if some quantitative differences have been observed for the height of the freak wave and the point of focusing. The experiments have been performed under strong wind, and with high values of initial steepness of the wave group, generating some spilling breakers. Hence, it has not been possible to reproduce exactly these experiments numerically. This can explain the deviations noticed previously. In order to provide quantitative comparisons, the next step should be to perform some new experi-

ments, using an initial wave train of smaller amplitude, to avoid breaking of the freak wave. Thus, it would be possible to reproduce these experiments numerically, and to obtain some quantitative comparisons.

Acknowledgements

The authors thank the referees for their useful comments and IRPHE for the computations assistance. The authors would also like to thank B. Zucchini and A. Laurence for their helpful technical assistance during the experiments.

References

[1] G. Lawton, Monsters of the deep (the perfect wave), New Scientist 170 (2297) (2001) 28–32.
[2] J.K. Mallory, Abnormal waves on the South-East Africa, Int. Hydrog. Rev. 51 (1974) 89–129.
[3] I.V. Lavrenov, The wave energy concentration at the Agulhas current of South Africa, Natural Hazards 17 (1998) (1974) 117–127.
[4] E. Pelinovsky, T. Talipova, C. Kharif, Nonlinear-dispersive mechanism of the freak wave formation in shallow water, Physica D 147 (2000) 83–94.
[5] A. Slunyaev, C. Kharif, E. Pelinovsky, T. Talipova, Nonlinear wave focusing on water of finite depth, Physica D 173 (2002) 77–97.
[6] K. Trulsen, K.B. Dysthe, Freak waves – A three-dimensional wave simulation, in: Proc. 21st Symp. on Naval Hydrodynamics, National Academy Press, 1997, pp. 550–560.
[7] A.R. Osborne, M. Onorato, M. Serio, The nonlinear dynamics of rogue waves and holes in deep water gravity wave train, Phys. Lett. A 275 (2000) 386–393.
[8] D. Clamond, J. Grue, Interaction between envelop solitons as a model for freak wave formation, C. R. Mecanique 330 (2002) 575–580.
[9] C. Kharif, E. Pelinovsky, Physical mechanisms of the rogue wave phenomenon, Eur. J. Mech. B Fluids 22 (2003) 603–634.
[10] H. Socquet-Juglard, K. Dysthe, K. Trulsen, H. Krogstad, Probability distributions of surface gravity waves during spectral changes, J. Fluid Mech. 542 (2005) 195–216.
[11] G.B. Whitham, Linear and Non Linear Waves, Willey & Sons, New York, 1974.
[12] A.M. Balk, The suppression of short waves by a train of long waves, J. Fluid Mech. 315 (1996) 139–150.
[13] J.P. Giovanangeli, C. Kharif, E. Pelinovsky, Experimental study of the wind effect on the focusing of transient wave group, in: Rogue Waves Proceedings, Rogue Waves (Brest, 2004).
[14] J. Miles, Surface wave generation: a viscoelastic model, J. Fluid Mech. 322 (1996) 131–145.
[15] H. Jeffreys, On the formation of water waves by wind, Proc. Roy. Soc. London Ser. A 107 (1925) 189–206.
[16] H. Jeffreys, On the formation of water waves by wind, Proc. Roy. Soc. London Ser. A 110 (1926) 241–247.
[17] N. Reul, H. Branger, J.P. Giovanangeli, Air flow separation over unsteady breaking waves, Phys. Fluids 11 (1999) 1959–1961.
[18] M.L. Banner, The influence of wave breaking on the surface pressure distribution in wind-wave interactions, J. Fluid Mech. 211 (1990) 463–495.
[19] M. Greco, A two-dimensional study of green water loading, PhD thesis, Dept. Marine Hydrodynamics, NTNU, Norway, 2001.
[20] T. Vinje, P. Brevig, Breaking waves on finite depth: a numerical study, Ship Res. Inst. Norway, R-118-81, 1981.
[21] D. Dommermuth, D. Yue, W. Lin, R. Rapp, E. Chan, W. Melville, Deep-water plunging breakers: a comparison between potential theory and experiments, J. Fluid Mech. 189 (1988) 423–442.